Acta Materialia 189 (2020) 1–11

Contents lists available at ScienceDirect

Acta Materialia

journal homepage: www.elsevier.com/locate/actamat

Matrix-precipitate interface-induced martensitic transformation within nanoscale phase field approach: Effect of energy and dimensionless interface width

Anup Basak[a], Valery I. Levitas*[,b,c]

[a] Department of Mechanical Engineering, Indian Institute of Technology Tirupati, Tirupati, A.P. 517506, India
[b] Departments of Aerospace Engineering, and Mechanical Engineering, Iowa State University, Ames, IA 50011, USA
[c] Division of Materials Science and Engineering, Ames Laboratory, Ames, IA 50011, USA

ARTICLE INFO

Article History:
Received 5 December 2019
Revised 4 February 2020
Accepted 19 February 2020
Available online 28 February 2020

Keywords:
Interface-induced martensitic transformation
Nucleation
Premartensite
Precipitate
Phase field approach
Finite strains

ABSTRACT

Martensitic transformation induced by the matrix-precipitate interface (or other internal surfaces) for single and two martensitic variants is studied using a thermodynamically consistent multiphase phase field approach. Three order parameters are considered; two of them describe the austenite (A) ↔ martensite (M) and variant M_i ↔variant M_j transformations in a matrix, and the third one describes the finite width matrix - non-transforming precipitate interface. The energy of the matrix-precipitate interface reduces during A → M phase transformation from the value for energy of A-precipitate interface, γ_A, to value for energy of M-precipitate interface, γ_M, due to its dependence on the order parameter related to the austenite↔martensite transformation. Such an interface increases the temperature for barrierless martensite nucleation well above the critical temperature for A → M transformation. The nucleation temperatures strongly depend on the ratio $\overline{\Delta}$ of the widths of the matrix-precipitates interface and A–M interface. New "phase diagram" for transformation temperatures between austenite, martensite, and premartensite versus $\overline{\Delta}$ has been presented for neglected mechanics for two cases when magnitude of $\Delta\gamma = \gamma_M - \gamma_A$ is larger than the energy of the A–M interface (0.2 N/m). For $\Delta\gamma = -0.5$ N/m, below a critical width ratio $\overline{\Delta}^*$, a layer of premartensite appears jump-like within the matrix-precipitate interface and progresses with reducing temperature, until it loses its stability and jump-like transforms to complete martensite in the entire matrix. However, for $\overline{\Delta} \geq \overline{\Delta}^*$, the entire matrix transforms to martensite without any premartensite. For $\Delta\gamma = -0.3$ N/m, no premartensite appears and the A matrix completely transforms into M at lower temperatures than the case with $\Delta\gamma = -0.5$ N/m. The combined effect of the energy of the matrix-precipitate interface, $\overline{\Delta}$, precipitation-induced misfit strains, and applied displacements on the boundary of the sample on nucleation of martensite and complex microstructure evolution in the systems with a single and two martensitic variant(s) is studied. Obtained results are important for controlling cyclic martensitic transformations in shape memory and elastocaloric alloys and designing alloys with desired characteristics of martensitic transformations.

1. Introduction

Foreign phase particles including the precipitates are frequently observed in crystalline solids, which can significantly affect the microstructure evolution during martensitic transformations (MTs) [1–5], plastic flow [6], solid↔melt transformations [7], and diffusion [7,8]. Thus, they determine various mechanical and transformational properties of the solids. With the advent of high resolution microscopes and powerful computers enabling researchers to perform atomistic simulations, it is now well-known that the interfaces in crystalline solids posses finite energy (excess energy according to Gibbs) and have finite width [7]. The solid-solid interfaces usually consist of few atoms to several tens of atoms across their width implying that the interface width might vary from several Å to several nanometers. The interfacial energy usually varies depending on its internal structure (e.g., interfacial dislocation density, misorientations of the adjacent phases) and ambient conditions (e.g. temperature); see e.g. Chapter 3 of [7]. The interactions between precipitates and matrix occur through the interfaces between them which possess energy and finite width, and also through the misfit strains at the interface, since the lattice parameters of matrix and precipitate usually differ; see e.g. Chapter 3 of [7]. Such interfaces between the precipitates and matrix play an important role in A↔M and $M_i \leftrightarrow M_j$ transformations which are the central phenomena in exhibiting the superelasticity and shape memory effects in various shape memory

* Corresponding author.
E-mail address: vlevitas@iastate.edu (V.I. Levitas).

https://doi.org/10.1016/j.actamat.2020.02.047
1359-6454/

alloys (SMAs) [1,9–12]. Here A, M, and M_i denote austenite, martensite, and i^{th} variant of martensite, respectively. Such an interface-induced phenomenon is actually driven by a decrease in the corresponding interface energy during phase transformation (PT). Premartensite (an intermediate state between A and M; see Section 2.1 for the exact definition) has been experimentally observed near the free surface in Cu-Zn-Al based alloys [10] and within NiAl alloys containing precipitates (see [1] and the references therein). The precipitates in SMAs are seen to significantly alter the MT temperatures, transformation paths, and hysteresis [1]. In Ni-Ti based alloys they also improve the fatigue strength under cyclic loadings, and thus increase the durability of the solid [13–15]. The misfit strains between the matrix and precipitates induce elastic stress fields which influence the nucleations of the martensitic phases and their kinetics [14,16]. Cuniberti et al. [2] showed that in a Cu-Al-Be SMA, an increase in the volume fraction of the γ_2-phase precipitates increases the martensitic transformation stress for $A \to M$ transformation. Similar observations were made by Baxevanis et al. [16,17] who considered a micromechanics based model to study the effect of precipitates on stress- and temperature-induced MTs in NiTi alloy using the finite element method (FEM) [18,19]. Otsuka and coworkers [20] showed that in NiTi alloys and in ferroelectric materials, the nano-size precipitates can yield a glassy type of behaviour of the solid. Multivariant MTs within the precipitates in NiTi alloys were studied by Li and Chen [4] experimentally, and Shi and Wang [21] using phase field method where they observed that the combined effect of applied load and the misfit strains due to precipitates can suppress evolution of some of the variants. The process of precipitation during aging and its effect on MTs and superelasticity behaviour was studied in SMAs experimentally [1,12,22] and using the phase field methods [23,24].

In spite of all these studies, the exact role of the finite-width matrix-precipitate interface on M nucleation and microstructure evolution is not yet well-understood. It is to be mentioned that the influence of sharp and diffuse external surfaces on premelting and melt↔solid transitions [25–28] and also on the nucleation of M and microstructure evolution [29,30] are studied with the phase field approach; see [31] for a review. The generic conclusions about the effect of the external surfaces are the followings. For a flat external surface, if the surface energy reduces during PT (for a given case, $\Delta\gamma^0 = \gamma_M^0 - \gamma_A^0 < 0$), the surface promotes $A \to M$ PT, and the transformation initiates below the critical temperature for lattice instability, where γ_M^0 and γ_A^0 are the energy of external surfaces of M and A phases, respectively. If reduction in surface energy exceeds the energy of phase interface (e.g., solid-melt or austenite-martensite interfaces), i.e., $\Delta\gamma^0 + \gamma_{0M} < 0$ with γ_{0M} for the energy of the austenite-martensite interface, then pretransformation starts from the surface even in the region of stability of the initial phase, e.g., below the equilibrium melting temperature for melting and above the martensite-austenite equilibrium temperature for martensitic PT.

The strong effect of the ratio of the width of an external surface to the width of a phase interface was first revealed in [30] for martensitic PT and then in [28] for melting, and in both the cases the processes are very complex (see also [32] and review [31]). The curvature of the interface promotes PT from the particle external surface [27,28] (because phase interface propagation reduces interface area and, consequently, energy) and suppresses PT from void [26]. Internal stresses generally suppress PT [29,30] but for some ratio of the width of the external surface to the width of the phase interface internal stresses promotes PT [30].

However, the effect of the ratio $\overline{\Delta}$ of width of the matrix-precipitates interface (denoted by δ_ξ) and width of the A – M interface (denoted by δ_{0M}), i.e. $\overline{\Delta} = \delta_\xi/\delta_{0M}$, and variable matrix-precipitate interface energy on martensite nucleation and transformations is not yet studied. The goal of this paper is to investigate the role of such interface parameters on nucleation of M, premartensitic transformations, and microstructure evolution within the systems with single variant and two variants using a phase field approach. A multiphase phase field approach of Ginzburg–Landau type, which assumes finite width for the interfaces, offers an ideal framework for such a study. The matrix-precipitate interface energy is assumed to vary between γ_M (precipitate-M matrix interface energy) to γ_A (precipitate-A matrix interface energy) during transformations. A system consisting of a square shaped non-transforming precipitate embedded in a transformable matrix is considered for detailed study in this paper; see Fig. 1(a) for a schematic. In particular, the effects of energy of the precipitate-matrix interface, S_0^i, width ratio $\overline{\Delta} = \delta_\xi/\delta_{0M}$, misfit strains, and external stresses are studied.

For our study, we consider a thermodynamically consistent multiphase phase field approach which is an extension of an approach recently developed by the authors in [33]. Three order parameters η_0, η_1, and ξ are assumed, where η_0 and η_1 describe the $A \leftrightarrow M$ and $M_i \leftrightarrow M_j$ transformations, respectively, and the order parameter ξ has been introduced to describe the finite-width interface between transformable matrix and the non-transformable precipitate. We assume that the precipitate lattice parameters differ from those of A and M_i and thus induces misfit strains during precipitation. The matrix-precipitate interface is considered to be stationary while the matrix undergoes martensitic transformations. Note that an order parameter similar to ξ was used to describe the material and surrounding vacuum (or gaseous medium) for studying external surface-induced melting in nanoparticles [26–28] and nanovoids [26], and surface-induced MTs in [30]. However, in the present study ξ describes two solid materials. While the small strain theory was considered in [30] for studying surface-induced MTs, the large strain approach is used in the present study and the structural stresses within all the interfaces are taken into account. Similar to [30] for the external surface, we assume that the matrix-precipitate interface energy varies during PT between γ_A and γ_M. The material parameters for NiAl are considered for numerical simulations. Notably, the Ni_3Al precipitates are often formed in NiAl alloy during various thermomechanical processes and such precipitates promote MTs [34]. The model presented in this paper is however general and applicable for any MT for a system with A and any two variants M_i and M_j. The first two martensitic variants M_1 and M_2 (i.e. the indices are $i = 1$ and $j = 2$) of NiAl alloy will be considered for simulations without loss of generality. We accept $\gamma_{0M} = 0.2$ N/m and for both values of $\Delta\gamma = -0.3$ N/m and –0.5 N/m under study, $\Delta\gamma + \gamma_{0M} < 0$ and pretransformation is thus expected; see Section 3 for a discussion about the material parameters. We will demonstrate that the results strongly depend on $\overline{\Delta}$.

First, the results for a thermal problem and neglected mechanics, with a single variant are presented assuming the system temperatures to be spatially uniform. A sophisticated transformation temperature θ versus the ratio $\overline{\Delta} = \delta_\xi/\delta_{0M}$ "phase diagram" describing the curves of transformations between A, premartensite PM, and M are presented for different energies of S_0^i. For $\Delta\gamma = -0.5$ N/m, below a critical value of the width ratio $\overline{\Delta} < \overline{\Delta}^*$, the austenite matrix transforms to M through appearance of PM. However, for $\overline{\Delta} > \overline{\Delta}^*$, the matrix directly transforms to M without any PM. However, when the magnitude of the difference in interface energy is relatively smaller, e.g. $\Delta\gamma = -0.3$ N/m, no PM is observed and the austenite matrix directly transforms to M and the nucleation and transformation temperatures (which are identical in this case) are significantly lower than that for $\Delta\gamma = -0.5$ N/m. Notably, in both the cases, all the transformation curves are well above the critical temperature for $A \to M$ transformation $\theta^c_{A\to M} = 0$ K of the solid (NiAl). Then considering mechanics, the effects of $\Delta\gamma$, misfit strains, width ratio $\overline{\Delta}$, and external loadings on barrierless nucleation and microstructure evolutions for a system with A and single variant M_1 and another system with A and two variants M_1 and M_2 are studied. We present the microstructures at the nucleation temperatures and also report the evolution of microstructures by reducing the temperatures of the system in steps.

As discussed in Section 3, the interfacial widths δ_{0M}, δ_{12}, and δ_{ξ} and the interfacial energy γ_{0M}, γ_{12}, and $\Delta\gamma$ are the input data to our phase field model. This is the only method which allows to study the effect of a finite-width interface on MTs while allowing to vary the width and energy of the interface independently without affecting the other system parameters and vice versa. The provision for studying the effect of $\overline{\Delta}$ is however not there in the sharp interface based approaches (e.g. level set approach [35]) where the interfacial width is taken as zero and the interfacial energy is considered to be just concentrated on the interface which is a lower dimensional manifold. Notably, in phase field approach by decreasing $\overline{\Delta}$ one can study the effect of matrix-precipitate interface on nucleation of M and MTs in the limit of sharp interface. This is also not possible using atomistic simulations, since the surface/interface energy and width are interrelated. The objective of the present study, i.e. study the effect of one of the parameters ($\overline{\Delta}$ or $\Delta\gamma$) keeping the other constant can be justified since it is well known that by engineering the surfaces/interfaces of crystals, their energy can be significantly modified; see e.g. [36].

The paper is organized as follows. In Section 2 the system of coupled elasticity and phase field equations is enlisted; the material parameters are listed in Section 3; the numerical results are presented in Section 4; finally, the paper is concluded in Section 5.

Notation: We denote the inner product and multiplication between two second-order tensors as $\boldsymbol{A} : \boldsymbol{B} = A_{ij}B_{ji}$ and $(\boldsymbol{A}\cdot\boldsymbol{B})_{ij} = A_{ik}B_{kj}$, respectively, where repeated indices denote Einstein's summation, and A_{ij} and B_{ij} are the components of the tensors in a right handed orthonormal Cartesian basis $\{\boldsymbol{e}_1, \boldsymbol{e}_2, \boldsymbol{e}_3\}$. The Euclidean norm of $\boldsymbol{A}$ is denoted as $|\boldsymbol{A}| = \sqrt{\boldsymbol{A} : \boldsymbol{A}^T}$; $\boldsymbol{I}$ is the second order identity tensor; $\boldsymbol{A}^{-1}$, $\boldsymbol{A}^T$, $det\,\boldsymbol{A}$, and $tr\boldsymbol{A}$ denote inversion, transposition, determinant, and trace of $\boldsymbol{A}$, respectively. Dyadic product between two arbitrary vectors $\boldsymbol{a}$ and $\boldsymbol{b}$ is denoted as $\boldsymbol{a}\otimes\boldsymbol{b}$. We denote the reference, intermediate (stress-free), and current configurations of a body by Ω_0, Ω_t, and Ω, respectively. The symbols ∇_0 and ∇ represent the gradient operators in the reference configuration Ω_0 and deformed configuration Ω, respectively; $\nabla_0^2 := \nabla_0\cdot\nabla_0$ and $\nabla^2 := \nabla\cdot\nabla$ are the Laplacian operators in Ω_0 and Ω, respectively. The symbol $:=$ stands for equality by definition.

2. System of coupled phase field and mechanics equations

In this section we describe the phase field model, which is a combination of large-strain multiphase phase field model in [33] and model in [26,28,30] for the stationary external surface, which is modified here to the model of stationary precipitate-matrix interface. The model presented in this section is general and applies to all MTs for the systems with austenite any two variants M_i and M_j. A brief description of the order parameters is given and the list of coupled elasticity and phase field equations are enlisted.

2.1. Order parameters

Three order parameters η_0, η_i, and ξ are considered, where η_0 and η_i are based on the transformation strains and describe the A $\leftrightarrow$ M and M_i $\leftrightarrow$ M_j transformations, respectively. Notably, the authors recently developed a general multiphase phase field approach in [33] where the same description of the order parameters η_0 and η_i have been used. We assume $\eta_0 = 0$ in A and $\eta_0 = 1$ in M; $\eta_i = 1$ in M_i and $\eta_i = 0$ in M_j. Note when $\eta_0 = 0$ at a material point, it is in A phase, while η_i may take any value between 0 and 1 at that point; see [33] for details. To describe a resultant microstructure with A and two variants, we define an equivalent order parameter $\eta_{eq} = 2\eta_0(\eta_i - 0.5)$. Clearly, when $\eta_{eq} = 1$, the material point is M_i; when $\eta_{eq} = -1$, the material point is M_j; when $\eta_{eq} = 0$, the material point is either A or lying on M_i–M_j interface. We consider that premartensite PM has nucleated in a particle if η_0 just attains 0.05 from a lower value, and complete martensitic transformation has occurred if η_0 just reaches and exceeds 0.95 from a lower value. Thus, a premartensite PM corresponds to $0.05 < \eta_0 < 0.95$.

The remaining order parameter ξ is used to describe the interface between non-transforming precipitate where $\xi = 0$, and the transformable matrix where $\xi = 1$. Note that $0 < \xi < 1$ within the precipitate-matrix interface. We would like to mention that a similar order parameter was used while studying external surface-induced solid-↔melt transformation in [26–28] and martensitic transformations in [30], where ξ described an interface between the material and surrounding environment. However, in the present paper ξ describes interface between two solids.

2.2. Kinematics

We denote the position vector of a particle in the deformed body Ω by $\boldsymbol{r}(\boldsymbol{r}_0, t)$, where $\boldsymbol{r} = \boldsymbol{r}_0 + \boldsymbol{u}(\boldsymbol{r}_0, t)$, $\boldsymbol{r}_0$, $\boldsymbol{u}$, and t denote the position vector in Ω_0, the displacement vector of the particle, and time instance, respectively. The total deformation gradient $\boldsymbol{F}$ is decomposed into

$$\boldsymbol{F} := \nabla_0\boldsymbol{r} = \boldsymbol{V}_e\cdot\boldsymbol{R}\cdot\boldsymbol{U}_t, \tag{2.1}$$

where the subscripts e and t stand for elastic and transformational parts, respectively, $\boldsymbol{U}_t$ is the symmetric right transformation stretch tensor, $\boldsymbol{V}_e$ is the symmetric left elastic stretch tensor, and $\boldsymbol{R}$ is the lattice rotation tensor. Also, we define $J = det\,\boldsymbol{F} := dV/dV_0$, $J_t = det\,\boldsymbol{U}_t := dV_t/dV_0$, and $J_e = det\,\boldsymbol{V}_e := dV/dV_t$, where dV_0, dV_t, and dV are infinitesimal volume elements in Ω_0, Ω_t, and Ω, respectively. Hence by Eq. (2.1), $J = J_tJ_e$. We will use the Eulerian total and elastic strain tensors as

$$\boldsymbol{b} = 0.5(\boldsymbol{V}^2 - \boldsymbol{I}), \quad \text{and} \quad \boldsymbol{b}_e = 0.5(\boldsymbol{V}_e^2 - \boldsymbol{I}), \tag{2.2}$$

respectively, where $\boldsymbol{V} = \sqrt{\boldsymbol{F}\cdot\boldsymbol{F}^T}$ is the left total stretch tensor.

2.3. Transformation stretch tensor

We consider the transformation stretch tensor $\boldsymbol{U}_t$ within the transformable matrix as a linear combination of the Bain strains multiplied with the interpolation functions of the order parameters [33]

$$\boldsymbol{U}_t = \boldsymbol{I} + \varphi(a_{\varepsilon}, \eta_0)[\boldsymbol{\varepsilon}_{tj} + \phi_i(\boldsymbol{\varepsilon}_{ti} - \boldsymbol{\varepsilon}_{tj})], \tag{2.3}$$

where $\boldsymbol{U}_{ti}$ and $\boldsymbol{\varepsilon}_{ti} = \boldsymbol{U}_{ti} - \boldsymbol{I}$ are the Bain stretch tensor and Bain strain tensor, respectively, for M_i. The interpolation functions $\varphi(a, \eta_0)$ and $\phi_i(\eta_i)$ are taken as [33]

$$\begin{aligned} &\varphi(a, \eta_0) = a\eta_0^2 + (4-2a)\eta_0^3 + (a-3)\eta_0^4, \\ &\text{and} \quad \phi_i = \eta_i^2(3-2\eta_i) = \varphi(3, \eta_i), \end{aligned} \tag{2.4}$$

respectively, and a is a constant parameter. Interpolation function ϕ_i is a particular case of φ that includes equivalence of variants M_i and M_j. The interpolation functions satisfy the following necessary conditions derived from the thermodynamic equilibrium of each phase [33]:

$$\begin{aligned} &\varphi(a, 0) = 0, \quad \varphi(a, 1) = 1, \quad \text{and} \quad \frac{\partial\varphi(a, 0)}{\partial\eta_0} = \frac{\partial\varphi(a, 1)}{\partial\eta_0} = 0; \\ &\phi_i(0) = 0, \quad \phi_i(1) = 1, \quad \text{and} \quad \frac{\partial\phi_i(0)}{\partial\eta_i} = \frac{\partial\phi_i(1)}{\partial\eta_i} = 0. \end{aligned} \tag{2.5}$$

2.4. Free energy

We consider the Helmholtz free energy per unit mass of the body in the following form (also see [33,37]):

$$\begin{aligned} \psi(\boldsymbol{F}, \eta_0, \eta_i, \xi, \theta, \nabla\eta_0, \nabla\eta_i, \nabla\xi) = {} & \frac{J_t}{\rho_0}\psi^e(\boldsymbol{b}_e, \eta_0, \eta_i, \theta) + J\check{\psi}^{\theta}(\eta_0, \eta_i, \theta) \\ & + \tilde{\psi}^{\theta}(\eta_0, \eta_i, \theta) + J\psi^{\nabla}(\nabla\eta_0, \nabla\eta_i) + \\ & J\psi^{\xi}(\xi, \nabla\xi, \eta_0, \eta_i), \end{aligned} \tag{2.6}$$

where ψ^e is the elastic strain energy per unit volume of Ω_t and we assume isotropic St. Venant–Kirchhoff elastic response of the solid, $\overset{\theta}{\psi}$ is the barrier energy related to A $\leftrightarrow$ M and $M_i \leftrightarrow M_j$ transformations, $\overset{\theta}{\tilde{\psi}}$ is the thermal energy, ψ^{∇} is the gradient energy, and the free energy ψ^{ξ} is the total of the barrier and gradient energy of the stationary interface between the precipitate and matrix (also see [30,33,37]):

$$\begin{aligned}
&\psi^e = \frac{\lambda}{2}(tr\,\boldsymbol{b}_e)^2 + \mu\,\boldsymbol{b}_e : \boldsymbol{b}_e;\\
&\overset{\theta}{\psi} = [A_{0M} + (a_\theta - 3)\Delta\psi^\theta(\theta)]\eta_0^2(1-\eta_0)^2 + \overline{A}\eta_i^2(1-\eta_i)^2\varphi(a_b,\eta_0);\\
&\overset{\theta}{\tilde{\psi}} = \psi_0^\theta(\theta) + \eta_0^2(3-2\eta_0)\Delta\psi^\theta(\theta);\\
&\psi^{\nabla} = \frac{1}{2\rho_0}[\beta_{0M}|\nabla\eta_0|^2 + \beta_{ij}|\nabla\eta_i|^2\tilde{\varphi}(a_\beta,a_0,\eta_0)];\\
&\psi^{\xi} = A_\xi\xi^2(1-\xi)^2 + \frac{1}{2\rho_0}\beta_\xi|\nabla\xi|^2, \quad A_\xi = \frac{18\gamma(\eta_0,\eta_i)}{\delta_\xi^2}, \quad \beta_\xi = \delta_\xi\gamma(\eta_0,\eta_i).
\end{aligned} \tag{2.7}$$

All the parameters appearing in Eq. (2.7) are defined here. λ and μ are the Lamé constants; A_{0M} is the barrier height between A and M, $\overline{A}$ is the barrier height between M_i and M_j, and A_ξ is the barrier height between the precipitate and matrix; $\Delta\psi^\theta = \psi_M^\theta - \psi_0^\theta = -\Delta s\,(\theta-\theta_e)$ is the thermal energy difference between A (denoted by ψ_0^θ) and M (denoted by ψ_M^θ), Δs is the change in entropy due to A to M transformation (assuming specific heats of A and M to be identical); $\theta > 0$ is the absolute temperature, and θ_e is the thermodynamic equilibrium temperature between A and M; β_{0M}, β_{ij}, and β_ξ are the gradient energy coefficients for A–M, M_i–M_j, and precipitate-matrix interfaces, respectively; $0 \le a_b, a_\beta, a_\theta \le 6$ [37] and $0 < a_0 \ll 1$ [33] are material constants. The interpolation function $\tilde{\varphi}$ in Eq. $(2.7)_4$ is taken as [33]

$$\begin{aligned}
\tilde{\varphi}(a_\beta,a_0,\eta_0) &= \varphi(a_\beta,\eta_0) + a_0\\
&= a_\beta\eta_0^2 + (4-2a_\beta)\eta_0^3 + (a_\beta-3)\eta_0^4 + a_0.
\end{aligned} \tag{2.8}$$

Note that in Eq. (2.6) the barrier energy and the gradient energy are multiplied with J and the gradient of η_0 and η_i are expressed in Ω to obtain the correct form the the structural stresses given by Eqs. $(2.18)_{3,4}$; see [33,37] for details. The precipitate-matrix interface energy is taken as (see [26–28,30])

$$\gamma = \gamma_A + \Delta\gamma\varphi(a,\eta_0), \tag{2.9}$$

where we have taken $a = 6$, and the parameters A_ξ and β_ξ appearing in Eq. (2.7) are expressed in terms of matrix-precipitate interface energy γ and width δ_ξ.

The material properties at any material point are determined using the following interpolation

$$\begin{aligned}
M(\eta_0,\eta_i,\theta,\boldsymbol{F}) = [(1-\varphi)M_0 + \Big(M_j + (M_i - M_j)\phi_i\Big)\varphi]\phi_\xi + M_p(1\\
-\varphi_\xi),
\end{aligned} \tag{2.10}$$

where M_0, M_i, M_j, and M_p are the properties of A, M_i, M_j, and precipitate, respectively, and

$$\phi_\xi = \xi^2(3-2\xi). \tag{2.11}$$

2.5. Dissipation rate and Ginzburg–Landau equations

Using a procedure similar to that in [33] (see Section 4 and Appendix A therein) and assuming that the dissipative stresses are zero, the following dissipation inequality is obtained

$$D = X_{0M}\dot{\eta}_0 + X_{ij}\dot{\eta}_i + X_\xi\dot{\xi} \ge 0, \tag{2.12}$$

which says that the total dissipation rate per unit volume D is summation of the rate of evolution of the order parameters multiplied by corresponding generalized conjugate forces given by

$$\begin{aligned}
X_{0M} &= (\boldsymbol{P}_e^T\cdot\boldsymbol{F} - J_t\psi^e\boldsymbol{I}) : \boldsymbol{U}_t^{-1}\cdot\frac{\partial\boldsymbol{U}_t}{\partial\eta_0} - J_t\frac{\partial\psi^e}{\partial\eta_0}\Big|_{\boldsymbol{F}_e} - \rho_0\Delta\psi^\theta(6\eta_0 - 6\eta_0^2) - \rho_0\overline{A}J\frac{\partial\varphi(a_b,\eta_0)}{\partial\eta_0}\eta_i^2(1-\eta_i)^2 -\\
&\quad \rho_0 J[A_{0M} + (a_\theta - 3)\Delta\psi^\theta(\theta)](2\eta_0 - 6\eta_0^2 + 4\eta_0^3) - \frac{J\beta_{ij}}{2}|\nabla\eta_i|^2\frac{\partial\tilde{\varphi}(a_\beta,a_0,\eta_0)}{\partial\eta_0} - \frac{\Delta\gamma}{\delta_\xi}\frac{\partial\varphi(a,\eta_0)}{\partial\eta_0}\times\\
&\quad \Big[18\xi^2(1-\xi)^2 + 0.5\delta_\xi^2|\nabla\xi|^2\Big] + \nabla_0\cdot(\beta_{0M}J\boldsymbol{F}^{-1}\cdot\nabla\eta_0),\\
X_{ij} &= (\boldsymbol{P}_e^T\cdot\boldsymbol{F} - J_t\psi^e\boldsymbol{I}) : \boldsymbol{U}_t^{-1}\cdot\frac{\partial\boldsymbol{U}_t}{\partial\eta_i} - J_t\frac{\partial\psi^e}{\partial\eta_i}\Big|_{\boldsymbol{F}_e} - \rho_0\overline{A}(2\eta_i - 6\eta_i^2 + 4\eta_i^3)\varphi(a_b,\eta_0) +\\
&\quad \nabla_0\cdot[J\tilde{\varphi}(a_\beta,a_0,\eta_0)\beta_{ij}\boldsymbol{F}^{-1}\cdot\nabla\eta_i], \quad \text{and}\\
X_\xi &= -A_\xi(2\xi - 6\xi^2 + 4\xi^3) - J_t\frac{\partial\psi^e}{\partial\xi}\Big|_{\boldsymbol{F}_e} + \nabla_0\cdot(\beta_\xi J\boldsymbol{F}^{-1}\cdot\nabla\xi).
\end{aligned} \tag{2.13}$$

Assuming that the dissipation rates due to the evolution of η_0, η_i, and ξ are decoupled, we rewrite the inequality (2.12) into $X_{0M}\dot{\eta}_0 \ge 0$, $X_{ij}\dot{\eta}_i \ge 0$, and $X_\xi\dot{\xi} \ge 0$ (which obviously satisfy the inequality (2.12)). We assume the following simplest linear kinetic equations which represent the Ginzburg–Landau equations:

$$\dot{\eta}_0 = L_{0M}X_{0M}, \quad \dot{\eta}_i = L_{ij}X_{ij}, \quad \text{and} \quad \dot{\xi} = L_\xi X_\xi, \tag{2.14}$$

where $L_{0M} > 0$, $L_{ij} > 0$, and $L_\xi > 0$ are the kinetic coefficients for A–M, M_i–M_j, and precipitate-matrix interfaces, respectively. For the order parameters we assume the homogeneous Neumann boundary conditions on all the external surfaces:

$$\nabla\eta_0\cdot\boldsymbol{n} = 0, \quad \nabla\eta_i\cdot\boldsymbol{n} = 0, \quad \text{and} \quad \nabla\xi\cdot\boldsymbol{n} = 0 \quad \text{on } S_0, \tag{2.15}$$

which mean that the energy of external surface does not change during phase transformations. In Eq. (2.15) $\boldsymbol{n}$ denotes the outward normal to the boundary in Ω. As mentioned in Section 1, we have considered only stationary matrix-precipitate interface in all our calculations related to martensitic transformations. The reason for still considering evolution of ξ in Eq. $(2.14)_3$ will be discussed in Section 4.

2.6. Mechanical equilibrium equation and stresses

The mechanical equilibrium equations are given by

$$\nabla_0\cdot\boldsymbol{P} = \boldsymbol{0} \quad \text{in } \Omega_0, \quad \text{or} \quad \nabla\cdot\boldsymbol{\sigma} = \boldsymbol{0} \quad \text{in } \Omega, \tag{2.16}$$

where $\boldsymbol{P}$ is the total first Piola–Kirchhoff stress tensor and $\boldsymbol{\sigma}$ is the total Cauchy stress tensor, which are decomposed into the elastic part and the structural parts (also see [30] for a small strain formulation):

$$\boldsymbol{P} = \boldsymbol{P}_e + \boldsymbol{P}_{st}^\eta + \boldsymbol{P}_{st}^\xi, \qquad \boldsymbol{\sigma} = \boldsymbol{\sigma}_e + \boldsymbol{\sigma}_{st}^\eta + \boldsymbol{\sigma}_{st}^\xi, \tag{2.17}$$

and the subscripts e and st stand for elastic and structural, respectively. The expressions for the stresses are [33]

$$\begin{aligned}
&\boldsymbol{P}_e = J_t\boldsymbol{V}_e^2\cdot\Big(\lambda\,tr(\boldsymbol{b}_e)\boldsymbol{I} + 2\mu\boldsymbol{b}_e\Big)\cdot\boldsymbol{F}^{-T}, \quad \boldsymbol{\sigma}_e = J_e^{-1}\boldsymbol{V}_e^2\cdot\Big(\lambda\,tr(\boldsymbol{b}_e)\boldsymbol{I} + 2\mu\boldsymbol{b}_e\Big),\\
&\boldsymbol{P}_{st}^\eta = J\rho_0(\overset{\theta}{\tilde{\psi}} + \psi^{\nabla})\boldsymbol{F}^{-T} - J\beta_{0M}(\nabla\eta_0\otimes\nabla\eta_0)\cdot\boldsymbol{F}^{-T} - J\tilde{\varphi}(a_\beta,a_0,\eta_0)\beta_{ij}(\nabla\eta_i\otimes\nabla\eta_i)\cdot\boldsymbol{F}^{-T},\\
&\boldsymbol{\sigma}_{st}^\eta = \rho_0(\overset{\theta}{\tilde{\psi}} + \psi^{\nabla})\boldsymbol{I} - \beta_{0M}\nabla\eta_0\otimes\nabla\eta_0 - \tilde{\varphi}(a_\beta,a_0,\eta_0)\beta_{ij}\nabla\eta_i\otimes\nabla\eta_i,\\
&\boldsymbol{P}_{st}^\xi = J\rho_0\psi^\xi\boldsymbol{F}^{-T} - J\beta_\xi(\nabla\xi\otimes\nabla\xi)\cdot\boldsymbol{F}^{-T}, \text{ and } \quad \boldsymbol{\sigma}_{st}^\xi = \rho_0\psi^\xi\boldsymbol{I} - \beta_\xi\nabla\xi\otimes\nabla\xi.
\end{aligned} \tag{2.18}$$

As it is shown in [33,37], such a thermodynamically consistent expression for structural stresses completely describe the interfacial biaxial tension with the resultant force equal to the interfacial energy.

The traction boundary conditions and the boundary displacements for the mechanics problem will be specified while presenting the numerical results in Section 4.

3. Material parameters

The free energy and the kinetic equations derived above involve several material parameters which need to be calibrated based on the experimental data or atomistic simulation results. Let us consider a simplified situation with neglected mechanics, i.e. $\psi^e = 0$ and $J = 1$,

which allows us to obtain the analytical solutions of the Ginzburg–Landau equations. We can then calibrate the material parameters such as the barrier heights, gradient energy coefficients, and kinetic coefficients using the known values of interfacial energy, width, and mobility.

Assuming that the interfaces are planar and the order parameters spatially vary with $r_{01} = \boldsymbol{r}_0 \cdot \boldsymbol{e}_1$ only and also that A_{0M}, $\overline{A}$, β_{0M}, and β_{ij} are constants, we simplify the Ginzburg–Landau equations in (2.14) for A–M (using $\eta_i = 1$ and $\xi = 1$) and M_i–M_j (using $\eta_0 = 1$) interfaces as

$$\frac{\dot{\eta}_0}{L_{0M}} = -\rho_0 \Delta\psi^{\theta}(6\eta_0 - 6\eta_0^2) - \rho_0 A_{0M}(2\eta_0 - 6\eta_0^2 + 4\eta_0^3) + \beta_{0M}\frac{\partial^2 \eta_0}{\partial r_{01}^2}, \quad \text{and}$$
$$\frac{\dot{\eta}_i}{L_{ij}} = -\rho_0 \overline{A}(2\eta_i - 6\eta_i^2 + 4\eta_i^3) + \beta_{ij}\frac{\partial^2 \eta_i}{\partial r_{01}^2}. \tag{3.1}$$

The solutions of the equations in (3.1) are [33,38]

$$\eta_0 = [1 + \exp(-\zeta_{0M})]^{-1}, \quad \text{and} \quad \eta_i = [1 + \exp(-\zeta_{ij})]^{-1}, \tag{3.2}$$

respectively, where

$$\zeta_{0M} = \frac{6}{\delta_{0M}}(r_{01} - r_{0c} - c_{0M}t), \quad \text{and} \quad \zeta_{ij} = \frac{6}{\delta_{ij}}(r_{01} - r_{0c} - c_{ij}t). \tag{3.3}$$

Here, the symbol δ denotes the width of the respective interface; γ denotes the interfacial energy, and c is the speed of interface propagation:

$$\delta_{0M} = \sqrt{\frac{18\beta_{0M}}{\rho_0 A_{0M}}}, \quad \delta_{ij} = \sqrt{\frac{18\beta_{ij}}{\rho_0 \overline{A}}}, \quad \gamma_{0M} = \frac{\beta_{0M}}{\delta_{0M}}, \quad \gamma_{ij} = \frac{\beta_{ij}}{\delta_{ij}},$$
$$c_{0M} = L_{0M}\delta_{0M}\Delta\psi^{\theta}(\theta), \quad c_{ij} = 0, \tag{3.4}$$

r_{0c} is the coordinate of a point where $\eta_0 = 0.5$ and $\eta_i = 0.5$ in the respective expressions, and obviously, the subscripts '$0M$' and 'ij' stand for $A - M$ and $M_i - M_j$ interfaces, respectively. The interfacial width is defined as the distance between points where corresponding order parameters take values between 0.05 and 0.95 [38]. Similarly, the analytical expression for stationary ξ (neglecting mechanics) is (see [30])

$$\xi = [1 + \exp(-\zeta_\xi)]^{-1}, \quad \text{where} \quad \zeta_\xi = \frac{6}{\delta_\xi}(r_0 - r_{0c}),$$
$$\delta_\xi = \sqrt{18\beta_\xi/\rho_0 A_\xi}, \quad \beta_\xi = \gamma_\xi \delta_\xi, \tag{3.5}$$

γ_ξ denotes the interfacial energy, and all other variables and parameters have similar meanings.

For all our calculations, we assume the material constants for NiAl alloy, in which A and M_i are cubic and tetragonal lattices, respectively; see [39–41] for the experimental and atomistic simulation based data. For our computations with two variants, we consider the variants M_1 and M_2 without loss of generality. The Bain tensors for M_1 and M_2 are [42]

$$\boldsymbol{U}_{t1} = diag(\alpha, \chi, \alpha) \quad \text{and} \quad \boldsymbol{U}_{t2} = diag(\chi, \alpha, \alpha), \tag{3.6}$$

respectively, where χ and α are material constants, and $diag(\alpha, \chi, \alpha)$, for example, denotes a 3×3 diagonal matrix with α, χ, and α as the respective diagonal elements with respect to an orthonormal Cartesian coordinate system where the axes are parallel to three mutually perpendicular sides of the cubic unit cell. See Fig. 2 for 2D representation of M_1 and M_2 unit cells in NiAl alloy. In all the simulations, we will consider $a_b = a_\beta = a_\theta = 3$, $a_0 = 10^{-3}$, $\delta_{0M} = 1$ nm, $\gamma_{0M} = 0.2$ N/m, $\delta_{12} = 0.58$ nm, $\gamma_{12} = 0.13$ N/m, $\Delta s = -5.58$ MPa/K, and $\theta_e = 215$ K. Using Eq. (3.4) and also the expressions for the critical temperatures (in Kelvin) for $A \to M$ and $M \to A$ transformations given by (see [43]) $\theta^c_{A\to M} = \theta_e + A_{0M}/(3\Delta s)$ and $\theta^c_{M\to A} = \theta_e - A_{0M}/(3\Delta s)$, respectively, we have $\theta^c_{A\to M} = 0$ K, $\theta^c_{M\to A} = 430$ K, $\rho_0 A_{0M} = 3600$ MPa, $\rho_0 \overline{A} = 4000$ MPa, $\beta_{0M} = 2 \times 10^{-10}$ N, and $\beta_{12} = 7.5 \times 10^{-11}$ N. The other parameters are taken to be $\lambda_0 = \lambda_1 = \lambda_2 = 74.6$ GPa, $\mu_0 = \mu_1 = \mu_2 = 72$ GPa (i.e. the elastic properties of A, M_1, and M_2 are identical), $\alpha = 0.922$, $\chi = 1.215$, and $L_{0M} = L_{12} = 2600$ (Pa-s)$^{-1}$. Since Ni_3Al precipitates are usually observed in NiAl alloy [34], we assume the elastic properties of Ni_3Al for the precipitate as $\lambda_p = 65$ GPa, $\mu_p = 70$ GPa; see e.g. [44] which reports anisotropic elastic constants for Ni_3Al. Note that the elastic moduli of the precipitate are close to that of the matrix (see e.g. [16]).

The energy of A-precipitate interface is taken to be $\gamma_A = 0.9$ N/m in all the simulations and we accept two values for $\Delta\gamma$, i.e. $\Delta\gamma = -0.3$ N/m and $\Delta\gamma = -0.5$ N/m, respectively. Although, in Refs. [36,45] we found that the free surface energy of cubic NiAl alloy (pure A) is usually close to 1.8 N/m, we could not find the exact values for γ_A and γ_M. Hence it is not possible for us to give an exact range for $\Delta\gamma$. Notably, Porter et al. [7] reports that the internal surface energy can vary between several mN/m to 1 N/m depending on the internal structure of the interface (e.g., density of interfacial dislocations, mutual orientation of adjacent phases) and ambient conditions (e.g. temperature). Furthermore, we know that by engineering the materials, the surface and interfacial energy can be modified as per requirements; see e.g. [36]. Hence $\Delta\gamma$ considered in this paper could possibly be achieved in practice.

We have taken the values for $\overline{\Delta}$ between 0.15 and 0.5 for all the simulations. We give the following explanation in support of it. The matrix-precipitate interface width δ_ξ usually varies between several Å to, say, one nanometer (see, e.g. Fig. (2 a) of [46] for a typical example in NiTi alloy). The values of δ_ξ depend on the structure of the interface (e.g., defect structure, misorientations between the crystals, and segregation of different species). On the other hand, δ_{0M} in most of the shape memory alloys is usually of several nanometers; see Chapter 7 of [42] and the references therein for experimental results and explanation based on the crystallographic theory of MTs. This justifies the range for $\overline{\Delta}$ considered here. While we take $\delta_{0M} = 1$ nm, $\delta_\xi = 0.15$ nm when $\overline{\Delta} = 0.15$. Although, in this case the computational cost is significantly high (see Section 4 for further discussion), it is still possible to get the results. Notably, the results for values of $\overline{\Delta}$ close to the lower range depicts the effect of matrix-precipitate interface on MTs in the limit of sharp interface.

4. Numerical results and discussions

First, we neglect the mechanics and report in Section 4.1 the results considering only thermal energy. The transformation temperatures versus width ratio $\overline{\Delta}$ plots have been presented showing the transformations between A, M, and PM for different values of $\Delta\gamma$. The microstructures are also shown. Then considering mechanics, the results for the systems with single variant and two variants are presented. Since the system under consideration (see Fig. 1(a)) has a four-fold symmetry with respect to the geometry and the loading condition, we just consider one quarter of the sample as shown in Fig. 1(b) for which the finite element computations are performed. For yielding the same result in this domain to what Fig. 1(a) would yield, at the boundary $r_{01} = 0$ we apply the displacement $u_1 = 0$ and on the boundary $r_{02} = 0$ we apply $u_2 = 0$; shear stresses are zero at both boundaries (see the roller supports on the respective faces in Fig. 1(b)). In all the simulations, the order parameter η_0 is constrained to 0 within the precipitate. However, no constraint has been imposed on η_1 and ξ.

In all the examples we have taken the sample size $l = 20$ nm and precipitate size $a = 2$ nm (Fig. 1(a)), i.e. the computations have been performed in a 10 nm × 10 nm domain (Fig. 1(b)). A large strain finite element code has been written in deal.ii which is an open source finite element package [47]. The plane stress condition is assumed when mechanics is considered. The FE procedure developed in [48] is utilized. We have used the quadratic quadrilateral elements for all our computations. The same mesh shown in Fig. 3(b) and (c) is used in all the examples where we have ensured that at least four grid

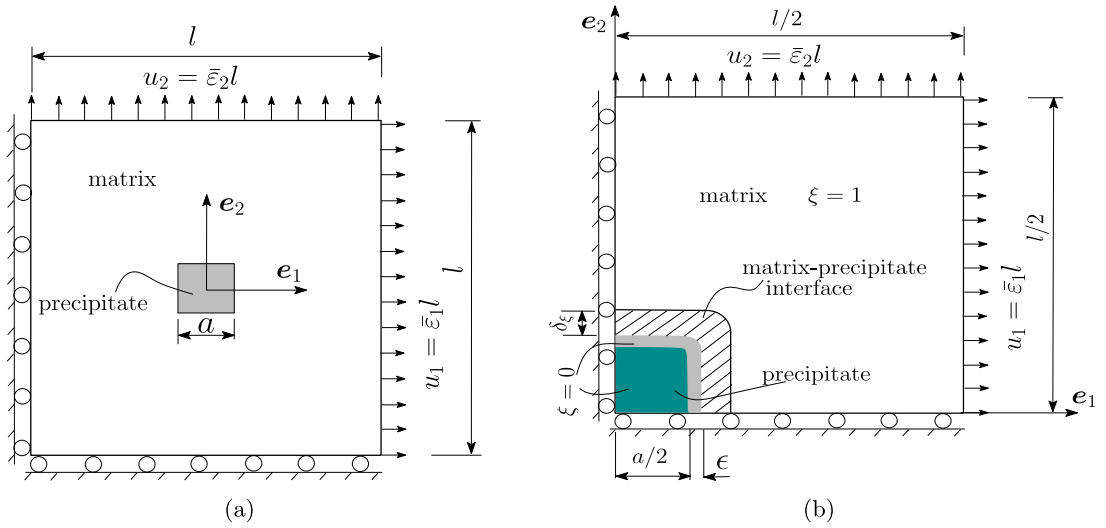

Fig. 1. (a) Schematic of the sample in the reference configuration Ω_0 with a precipitate (shaded region) and matrix. (b) A quarter of the sample shown in Fig. 1(a), where the finite element computation is performed. The green region is the precipitate, and the grey region (exaggerated for visual) is a part of the computational domain where large values of the driving force X_{0M} are concentrated as discussed in Section 4.

points are present across all the interfaces. We have done all the simulations for $\overline{\Delta}$ ranging between 0.15 and 0.5. However, one can consider $\overline{\Delta} < 0.15$ with a more refined mesh.

To achieve a smooth matrix-precipitate interface as shown in Fig. 1(b), we have considered two rectangular regions of width δ_ξ (exact values specified while presenting results) above the horizontal and vertical surfaces of the precipitate, which intersect near the corner. We then let only ξ evolve according to Eq. $(2.14)_3$ for four time steps with step size $\Delta t = 10^{-15}$ s so that we get the smooth matrix-precipitate interface near the corner (as shown in Fig. 1(b)). Once the smooth matrix-precipitate interface is obtained, then we solve for η_0 and η_1 using Eq. $(2.14)_{1,2}$ to study the effect of stationary matrix-precipitate interface on MTs.

It is to be noted that since we constrained η_0 to 0 within the precipitate (dark green region in Fig. 1(b)), there is a concentration of large values of the driving force X_{0M} within a small region of size $\epsilon \sim 0.1$ nm around the boundary lines between the precipitate and matrix (shown exaggeratedly for visual as grey region in Fig. 1(b)). This is simply because of sharp change in η_0 from the dark green region to adjacent part of the matrix, and hence should be viewed as an numerical artefact. This driving force does not vanish and remains almost constant during the subsequent simulation. To avoid any computational error due to such concentration of X_{0M} within the grey region, we take the matrix-precipitate interface beyond that small region as shown by hatched area in Fig. 1(b). For all the examples below, we have taken $\epsilon = 0.16$ nm.

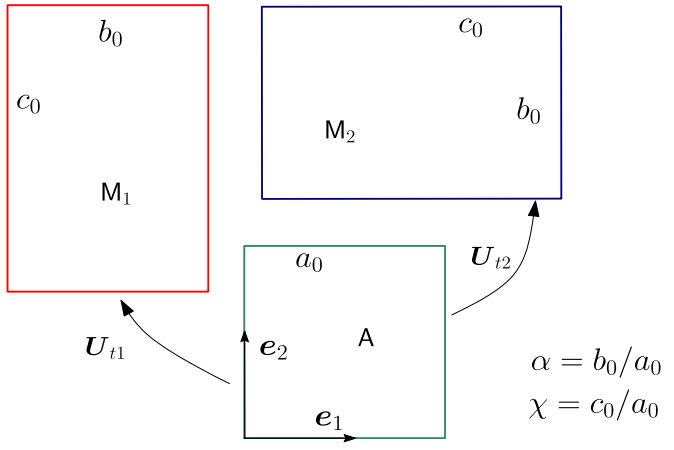

Fig. 2. Unit cells of the cubic austenite and two tetragonal martensitic variants M_1 and M_2 in 2D with respect to the basis $\{e_1, e_2\}$, where the axes are parallel to the sides of the cubic A unit cell.

4.1. Results with neglected mechanics

Here we present the results for a system with austenite and a single variant M_1 when mechanics is not considered, i.e. MT is induced by the matrix-precipitate interface and temperature. The Ginzburg–Landau equation for η_0 Eq. $(2.14)_1$ with setting $\eta_1 = 1$ simplifies to

$$\frac{\dot{\eta}_0}{L_{0M}} = -\rho_0 \Delta\psi^\theta (6\eta_0 - 6\eta_0^2) - \rho_0 A_{0M}(2\eta_0 - 6\eta_0^2 + 4\eta_0^3) - \frac{\Delta\gamma}{\delta_\xi}\frac{\partial\varphi(a,\eta_0)}{\partial\eta_0}\left[18\xi^2(1-\xi)^2 + 0.5\delta_\xi^2|\nabla\xi|^2\right] + \beta_{0M}\nabla_0^2\eta_0. \tag{4.1}$$

The stationary order parameters η_0 for varying temperatures along a line $r_{02} = 0.5$ nm in the sample (see Fig. 1(b)) for $\Delta\gamma = -0.5$ N/m and $\delta_\xi = 0.15$ nm are shown in Fig. 3(a). At $\theta = 181.7$ K the A matrix does not transform. After the temperature is reduced by 0.1 K, PM appears discontinuously adjacent to the precipitate. This temperature is considered as A → PM transformation temperature. As the temperature is further reduced, the stationary region occupied by the PM becomes wider and wider until $\theta = 168$ K, at which jump completely transformed martensite occurs in the matrix. This temperature is designated as PM → M transformation temperature. The stationary distribution of the PM is shown in Fig. 3(b) (a part of the sample is shown therein) when $\theta = 175$ K. The stationary ξ is also shown in Fig. 3(c) for $\delta_\xi = 0.15$ nm. In the Figs. 3(b) and (c) the mesh density is shown. A denser mesh is considered near the precipitate and the mesh is coarser away from it.

The temperature θ versus $\overline{\Delta}$ plots for the transformation curves between A, M, and PM are shown in Fig. 4(a) and (b) for $\Delta\gamma = -0.5$ N/m and $\Delta\gamma = -0.3$ N/m, respectively, which are obtained by varying the width of S_0^i. In Fig. 4(a) we see that for $0.15 \le \overline{\Delta} \le \overline{\Delta}^* = 0.2$, the MT (curve PM → M) occurs through appearance of the premartensite as the temperature is decreased from austenite phase. We call $\overline{\Delta}^*$ as the critical width ratio. When $\overline{\Delta} > \overline{\Delta}^*$, A directly transforms into M without any PM. From Fig. 4(a) we note that the A → PM transformation curve (for $\overline{\Delta} \le \overline{\Delta}^*$) is a monotonically decreasing function of $\overline{\Delta}$

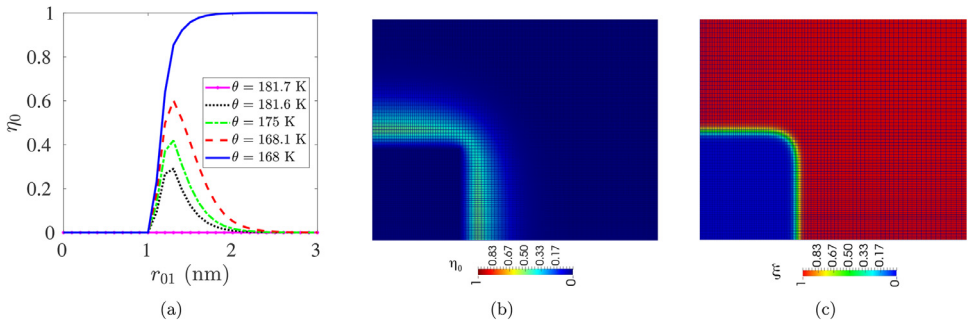

Fig. 3. Stationary solution for neglected mechanics for $\Delta\gamma = -0.5$ N/m and $\delta_\xi = 0.15$ nm (i.e. $\overline{\Delta} = 0.15$). (a) The order parameter η_0 profile along the $r_{02} = 0.5$ nm line in the sample for varying temperatures. (b) and (c) Part of the sample with the stationary distributions for η_0 and ξ, respectively, for $\theta = 175$ K. Figs. (b) and (c) also show variation of finite element mesh density.

whereas PM → M is an increasing function of $\overline{\Delta}$. That is the transformation temperature to M (including PM) is an increasing function of $\overline{\Delta}$ for $\overline{\Delta} \le \overline{\Delta}^*$ and it is a decreasing function for $\overline{\Delta} > \overline{\Delta}^*$. All the transformation temperatures are significantly above the critical temperature for A to M transformation $\theta^c_{\mathrm{A}\to\mathrm{M}} = 0$ K, which clearly indicates that reduction in matrix-precipitate interface energy promotes the transformation.

In order to understand the effect of $\Delta\gamma$ we have also performed the simulations for $\Delta\gamma = -0.3$ N/m while all other parameters are the same as for the case with $\Delta\gamma = -0.5$ N/m. The transformation curve is shown in Fig. 4(b). Obviously, over the entire range $0.15 \le \overline{\Delta} \le 0.5$, A transforms into M without any PM. Up to $\overline{\Delta} = 0.34$, the transformation temperature increases monotonically, but after that it becomes almost constant. In this case also all the A → M transformation temperatures are much above the critical temperature $\theta^c_{\mathrm{A}\to\mathrm{M}} = 0$ K, but they are significantly lower than the transformation temperatures for $\Delta\gamma = -0.5$ N/m. We considered also the case when $\Delta\gamma = 0$ and found that all the A → M transformation temperatures are very close to the $\theta^c_{\mathrm{A}\to\mathrm{M}} = 0$ K which is expected.

4.2. Results with for coupled phase field and mechanics

We now present the results when the mechanics is also taken into consideration, first for a system with A and a single variant M_1 and then for a system with A and two variants M_1 and M_2. The sample with the displacement boundary conditions is shown in Fig. 1(b). The prescribed normal displacements at the boundary correspond to the values of averaged strain values of $\overline{\varepsilon}_1$ and $\overline{\varepsilon}_2$, which will be specified for each example. In all the following examples we have selected the misfit strain tensor between inclusion and matrix as $diag(-0.01, -0.01)$.

4.2.1. System with A and M_1

We consider a system with A and M_1. The transformation stretch tensor and the non-trivial Ginzburg-Landau equation are obtained using $\eta_1 = 1$ from Eqs. (2.3) and $(2.13)_1$:

$$\boldsymbol{U}_t = \boldsymbol{I} + (\boldsymbol{U}_{t1} - \boldsymbol{I})\varphi(a_\varepsilon, \eta_0), \quad \text{and} \tag{4.2}$$

$$\frac{\dot{\eta}_0}{L_{0M}} = (\boldsymbol{P}_e^T \cdot \boldsymbol{F} - J_t \psi^e \boldsymbol{I}) : \boldsymbol{U}_t^{-1} \cdot \frac{\partial \boldsymbol{U}_t}{\partial \eta_0} - J_t \frac{\partial \psi^e}{\partial \eta_0}\Big|_{\boldsymbol{F}_e} - \rho_0 \Delta\psi^\theta (6\eta_0 - 6\eta_0^2) - \rho_0 A_{0M} J (2\eta_0 - 6\eta_0^2 + 4\eta_0^3) - \frac{\Delta\gamma}{\delta_\xi} \frac{\partial\varphi(a,\eta_0)}{\partial\eta_0} \left[18\xi^2(1-\xi)^2 + 0.5\delta_\xi^2 |\nabla\xi|^2\right] + \nabla_0 \cdot (\beta_{0M} J \boldsymbol{F}^{-1} \cdot \nabla\eta_0), \tag{4.3}$$

respectively (recall that $a_\theta = 3$). The Bain tensor $\boldsymbol{U}_{t1}$ given by Eq. $(3.6)_1$ is used in Eqs. (4.2) and (4.3). We have done the simulations in a domain shown in Fig. 1(b), where η_0 is constrained to 0 and the initial condition in the matrix is taken to be $\eta_0 = 0.01$. The simulation results for three different sets of parameter values are presented.

Case-I. $\Delta\gamma = -0.5$ N/m and $\overline{\varepsilon}_1 = \overline{\varepsilon}_2 = 0$.

At $\theta = 182$ K the nucleation of the product phase takes place near the horizontal face of the precipitate as shown in Fig. 5 (i), however, the rest of the matrix is in austenite phase. Since the maximum value of η_0 (stationary solution) at that temperature is 0.41, the product phase is obviously the PM. Above $\theta = 182$ K, no PM was seen and the matrix was in A phase. Note that the PM appears at the nucleation temperature at the horizontal interface between the matrix and precipitate, but no nucleation occurs at the vertical interface. Noticing the orientation of the unit cell of M_1 from Fig. 2, we can say that the combined effect of the interface energy and the misfit strains (compressive within the precipitate) promotes the nucleation of M_1 on that horizontal interface and suppresses the nucleation on the vertical matrix-precipitate interface at $\theta = 182$ K. However, as the

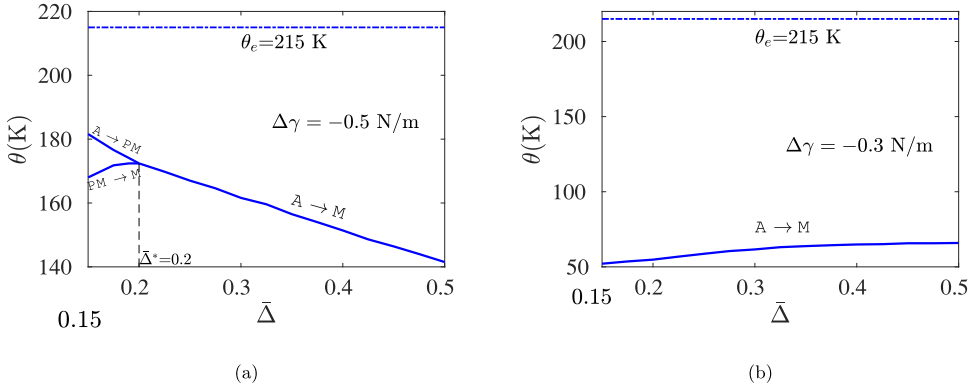

Fig. 4. Transformation temperatures versus width ratio $\overline{\Delta}$ for a system with A and a single M variant with neglected mechanics for (a) $\Delta\gamma = -0.5$ N/m and (b) $\Delta\gamma = -0.3$ N/m.

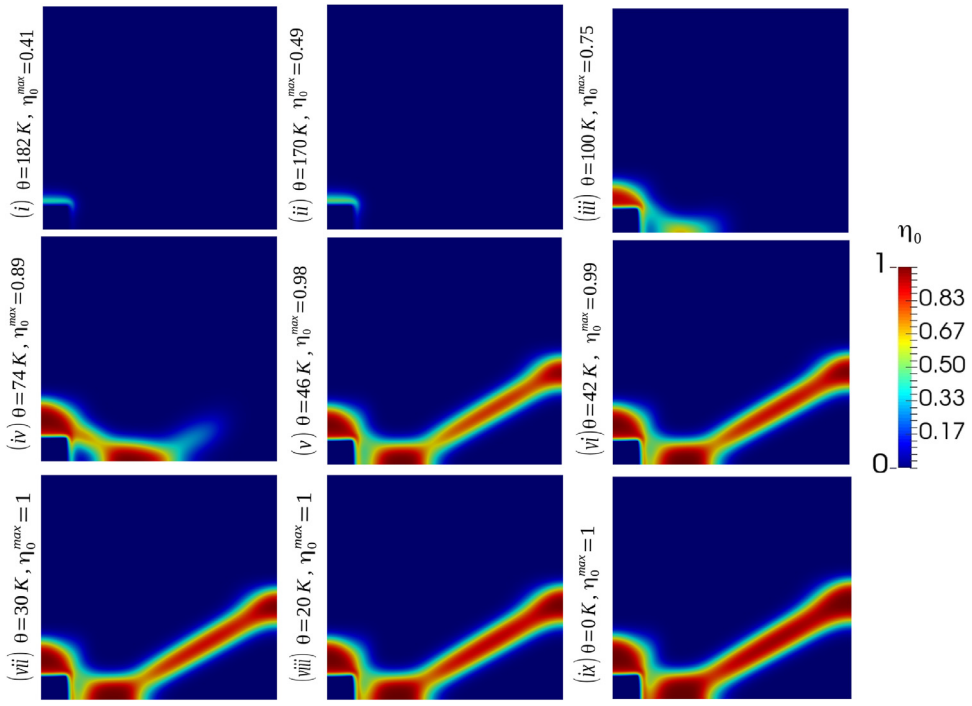

Fig. 5. Stationary solutions for η_0 in a system with single martensitic variant M_1 at different temperatures in the deformed configuration Ω when mechanics is considered. The misfit normal strains (normal) in $\boldsymbol{e}_1$ and $\boldsymbol{e}_2$ directions are –1%. Fig. (i) shows the solution at the nucleation temperature 182 K. The maximum value of η_0 for each of the stationary solutions is mentioned.

temperature decreases, the PM appears on the vertical interface as well; see Figs. 5(ii)–(iv). M_1 reaches at the horizontal bottom surface of the sample as well. As the temperature decreases, an inclined martensitic band forms and grows as shown in Figs. 5(v)–(ix). While in Figs. 5 (ix) temperature reaches instability temperature of A for stress-free case, geometric constraint $\bar{\varepsilon}_1 = \bar{\varepsilon}_2 = 0$ retains major part of the sample in austenitic phase.

Case-II. $\Delta\gamma = -0.5$ N/m and $\bar{\varepsilon}_1 = \bar{\varepsilon}_2 = 0.02$.

All other parameters are the same as for the case with $\bar{\varepsilon}_1 = \bar{\varepsilon}_2 = 0$, i.e. Case-I. The nucleation temperature in this case is $\theta = 255$ K which is higher than the case with $\bar{\varepsilon}_1 = \bar{\varepsilon}_2 = 0$, implying that the tensile external stresses promote nucleation. The microstructure evolution is qualitatively similar to that shown in Fig. 5 (of course at different temperatures) and hence not shown here.

Case-III. $\Delta\gamma = -0.3$ N/m and $\bar{\varepsilon}_1 = \bar{\varepsilon}_2 = 0$.

We have also done the simulations with $\Delta\gamma = -0.3$ N/m and $\bar{\varepsilon}_1 = \bar{\varepsilon}_2 = 0$, while all other parameters are identical with Case-I and Case-II. The nucleation starts in this case at 77 K near the horizontal interface (similar to Fig. 5(i)). Obviously, the nucleation temperature is much lower than the case with $\Delta\gamma = -0.5$ N/m, as expected. The microstructure evolution is qualitatively similar to the case $\Delta\gamma = -0.5$ N/m shown in Fig. 5 and not shown here.

4.2.2. *System with* A *and two variants* M_1 *and* M_2

The Bain tensors given by Eq. (3.6) are considered in the transformation stretch tensor in Eq. (2.3), where the orientation of all the unit cells are shown in Fig. 2. We imposed $\bar{\varepsilon}_1 = \bar{\varepsilon}_2 = 0$ for all the examples with two variants. Results for $\Delta\gamma = -0.5$ N/m and $\Delta\gamma = -0.3$ N/m are shown.

Case-a. $\Delta\gamma = -0.5$ N/m

In Fig. 6 the stationary microstructures are shown for three temperatures in three columns. Three rows show the plots for η_0, η_1, and η_{eq}, respectively. The nucleation of M occurs at $\theta = 182$ K on both the vertical and horizontal matrix-precipitate interfaces, i.e. the nucleation temperature remains the same for the cases with single and two variants (compare with the results in Section 4.2.1). Since the misfit strains are compressive and the unit cells of the variants are oriented as shown in Fig. 2, the variant M_1 is expected to be promoted on the horizontal matrix-precipitate interface and the variant M_2 is expected to be promoted on the vertical interface. The simulation results shown in Fig. 6 are thus consistent. At the nucleation temperature $\theta = 182$ K, PM is seen with $\eta_0^{max} = 0.35$ (top-left corner figure). If the temperature is decreased to $\theta = 150$ K, still we see PM with $\eta_0^{max} = 0.54$. If the temperature is further decreased, say to $\theta = 50$ K, the microstructure shown in the third column of Fig. 6 is obtained. The degree of undercooling $(\theta_e - 50)\ K\ = 165$ K results into a larger volume of M. The martensitic plates of both the variants are oriented at 45° with respect to the $\boldsymbol{e}_1$ direction, which can be explained using the solutions of the twinning equation from the crystallographic theory of martensite; see e.g. Chapter 5 of [42] and also see [33] for phase field simulations. While microstructure is not symmetric with respect to exchange of martensitic variants, the volume fraction of the variants is approximately equal, as expected. If the external forcing is applied (e.g. nonzero $\bar{\varepsilon}_1$ and $\bar{\varepsilon}_2$), the nucleation temperatures can be further increased or decreased depending on the signs of the forcing, similar to that discussed above for the single variant.

Case-b. $\Delta\gamma = -0.3$ N/m

We have also done the simulation with $\Delta\gamma = -0.3$ N/m. The nucleation occurs at 77 K which is same as the nucleation temperature for the system with single variant. The stationary microstructure at that temperature is shown in Fig. 7, which consists of martensitic plates adjacent to the matrix-precipitate interfaces and martensitic plates of alternative variants which are inclined at 45° with respect to horizontal surface of the sample.

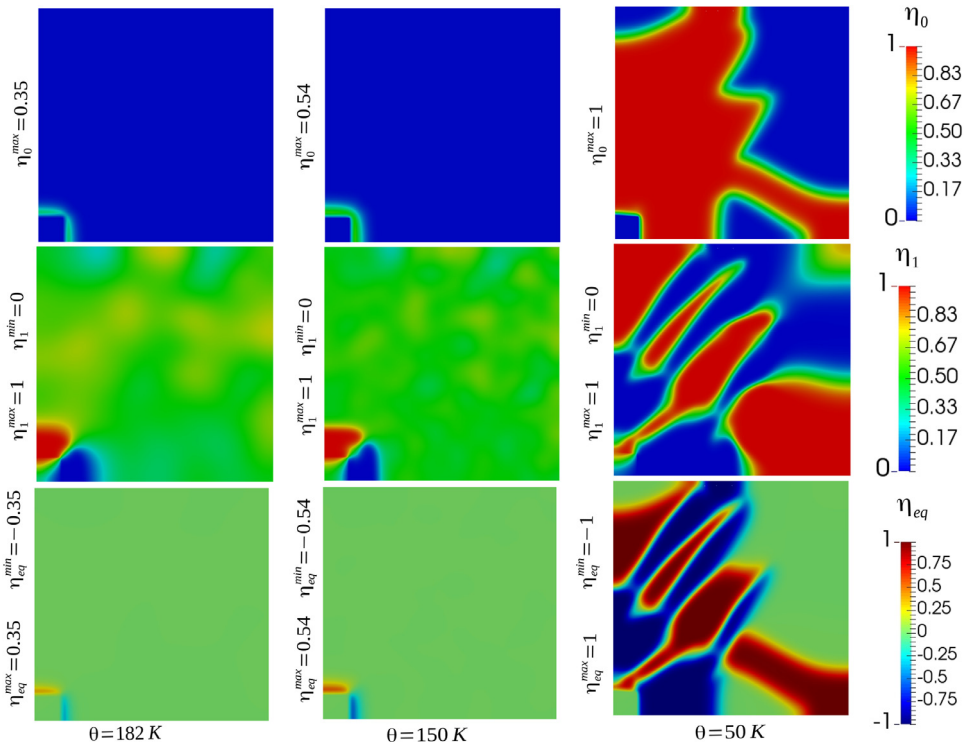

Fig. 6. Stationary microstructures in a system with A and two martensitic variants M_1 and M_2 at different temperatures for $\Delta\gamma = -0.5$ N/m. The three rows show the solutions for η_0, η_1, and η_{eq}, respectively. The three columns show the results at temperatures $\theta = 182$ K (nucleation temperature), $\theta = 150$ K, and $\theta = 50$ K, respectively. The misfit normal strains considered in $\boldsymbol{e}_1$ and $\boldsymbol{e}_2$ directions are –0.01. The maximum values of η_0, η_1, and η_{eq} for each of the solutions are reported.

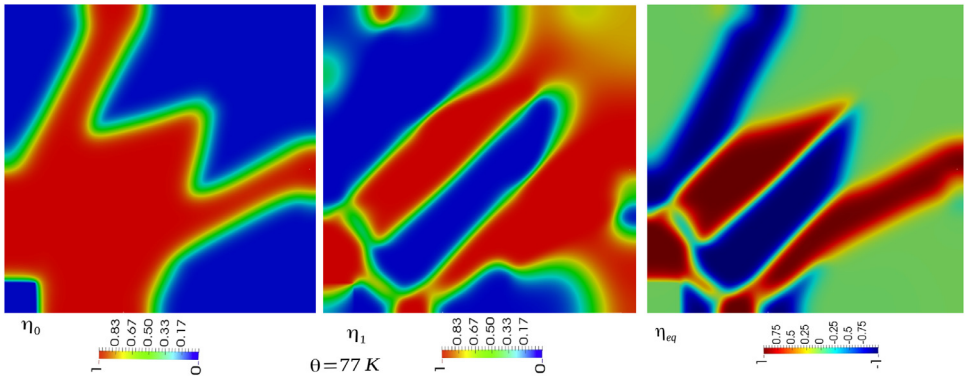

Fig. 7. Stationary microstructure for a system with two variants for $\Delta\gamma = -0.3$ N/m at the nucleation temperature $\theta = 77$ K. The misfit normal strains in $\boldsymbol{e}_1$ and $\boldsymbol{e}_2$ directions are –0.01.

5. Conclusions

A detailed computational study of a matrix-precipitate interface induced martensitic transformation within the matrix is presented using a thermodynamically consistent multiphase phase field approach. Two order parameters describing the A ↔ M and $M_i \leftrightarrow M_j$ transformations are involved, and another order parameter describing the interface between the transformable matrix and non-transformable precipitate is included. Change in matrix-precipitate interfacial energy during phase transformation is taken into account utilizing a variable energy of the interface as a function of the order parameter related to the austenite↔martensite transformation. Since for both cases under study, matrix-precipitate interfacial energy reduces during martensitic transformation, and the magnitude of this reduction $|\Delta\gamma| = 0.5$ and 0.3 N/m is larger than the A–M interfacial energy $\gamma_{0M} = 0.2$ N/m, all the barrierless A → PM and A → M transformation temperatures are well above the critical temperature for A → M transformation (0 K). In addition, the strong effect of the ratio $\overline{\Delta}$ of the matrix-precipitate interface width and the austenite-martensite interface width is found. The transformation initiation curves between austenite, martensite, and premartensite as a function of the ratio $\overline{\Delta}$ are plotted by varying the matrix-precipitate interface width for neglected mechanics (Fig. 4). For $\Delta\gamma = -0.5$ N/m, below a critical width ratio $\overline{\Delta} \leq \overline{\Delta}^*$, the austenite matrix transforms to martensite via a premartensite appearing near the interface. However, for $\overline{\Delta} > \overline{\Delta}^*$, no PM is seen, rather a complete martensite nucleates at the interface and the entire matrix transforms into M at the nucleation temperature only. For $\Delta\gamma = -0.3$ N/m, A directly transforms into M without any premartensite.

Finally, the effects of mechanics, namely, internal stresses due to transformation strain in martensitic variants, misfit strains between precipitate and matrix, and external stresses (applied displacements) are investigated. Nucleation of martensite in the systems with single and two variants occurs at the same temperature, provided that all

other conditions are the same. This happens because different faces of the precipitates promote different martensitic variants, which do not interact at the nucleation stage. The microstructure evolution is also studied for these two systems by reducing the temperatures in steps from the nucleation temperature and reaching stationary solutions.

Obviously, the effect of parameter $\overline{\Delta}$ on initiation of PTs is multifaceted, complex, and depends on other parameters such as $\Delta\gamma$ and misfit strain, and is often counter-intuitive. For example, according to Fig. 4(a), when $\Delta\gamma = -0.5$ N/m, an increase in $\overline{\Delta}$ suppresses loss of stability of A because the total promoting energy gain $\Delta\gamma$ is distributed along a wider precipitate-matrix interface resulting in a smaller maximum local energy gain. However, for $\overline{\Delta} \leq \overline{\Delta}^*$, A transforms gradually to PM, while for $\overline{\Delta} > \overline{\Delta}^*$, the PM does not appear and A transforms directly to M. At the same time, an increase in $\overline{\Delta}$ promotes transformation of PM to M, which is difficult to rationalize based on a simple energetic arguments.

The formation of premartensite and subsequent M transformations near the external surface [10] and in the presence of internal surfaces such as matrix-precipitate interface and grain boundaries (see e.g. [1] and the references therein) have been observed in experiments. However, we cannot give any quantitative comparison here as we do not have any suitable experimental data.

Notably, the effects of the parameters such as reduction of the matrix-precipitate energy and ratio of the width of the matrix-precipitate to the austenite-martensite interface were never studied within phase field approach. Loss of interface coherency and interaction of generated dislocations with MT can also be included in the present approach using models developed in [49,50]. Obtained results are important for controlling cyclic martensitic transformations in shape memory and elastocaloric alloys and designing alloys with desired characteristic of martensitic transformations [13–15].

Note that in all previous works [26–32], while studying the effect of the parameter $\overline{\Delta}$ on different kinds of PTs (which, of course, do not include the nucleation at a precipitate), $\overline{\Delta}$ was varied over a broad range to get a conceptual idea about its influence, since the actual range for $\overline{\Delta}$ was not yet measured. We hope that the theoretical works in [26–32] and in the present paper will promote interest in the experimental studies.

Declaration of interests

The authors declare that they have no known competing financial interests or personal relationships that could have appeared to influence the work reported in this paper.

Acknowledgments

Support of NSF (CMMI-1536925 and MMN-1904830) and Iowa State University (Vance Coffman Faculty Chair Professorship) is gratefully acknowledged. Simulations were performed at Extreme Science and Engineering Discovery Environment (XSEDE), allocation TG-MSS140033.

References

[1] K. Otsuka, X. Ren, Physical metallurgy of TiNi-based shape memory alloys, Prog. Mater. Sci. 50 (2005) 511–678.
[2] A. Cuniberti, S. Montecinos, F.C. Lovey, Effect of γ_2-phase precipitates on the martensitic transformation of a β-CuAlBe shape memory alloy, Intermetallics 17 (2009) 435–440.
[3] N. Zhou, C. Shen, M.F.-X. Wagner, G. Eggeler, M.J. Mills, Y. Wang, Effect of Ni_4Ti_3 precipitation on martensitic transformation in TiNi, Acta Mater. 58 (2010) 6685–6694.
[4] D.Y. Li, L.Q. Chen, Selected variant growth of coherent $Ti_{11}Ni_{14}$ precipitate in a TiNi alloy under applied stresses, Acta Mater. 45 (1997) 471–479.
[5] D. Stroz, D. Chrobak, Effect of internal strain on martensitic transformations in NiTi shape memory alloys, Mater. Trans. 52 (2011) 358–363.
[6] H. Sehitoglu, T. Foglesong, H.J. Maier, Precipitate effects on the mechanical behavior of aluminum copper alloys: part i. experiments, Metall. Mater. Trans. A. 36 (2005) 749–761.
[7] D.A. Porter, K.E. Easterling, M.Y. Sherif, Phase Transformations in Metals and Alloys, CRC Press, Boca Raton, 2009.
[8] W. Guo, I. Steinbach, C. Somsen, G. Eggeler, On the effect of superimposed external stresses on the nucleation and growth of Ni_4Ti_3 particles: a parametric phase field study, Acta Mater. 59 (2011) 3287–3296.
[9] J. Diao, K. Gall, M.L. Dunn, Surface-stress-induced phase transformation in metal nanowires, Nat. Mater. 2 (2003) 656–660.
[10] F.C. Lovely, M. Chandrasekaran, Diffraction effects in CuZn and Cu-Zn-Al: surface martensite transformation and microstructure, Acta Matall. 31 (1983) 1919–1927.
[11] M. Ahlers, Martensite and equilibrium phases in Cu-Zn and Cu-Zn-Al alloys, Prog. Mater. Sci. 30 (1986) 135–186.
[12] J. Pons, E. Cesari, Martensitic transformation cycling in a β Cu-Zn-Al alloy containing γ-precipitates, Acta Matall. Mater. 41 (1993) 2547–2555.
[13] K. Gall, H.J. Maier, Cyclic deformation mechanisms in precipitated NiTi shape memory alloys, Acta Mater. 50 (2002) 4643–4657.
[14] C. Chluba, W. Ge, R.L. Miranda, J. Strobel, L. Kienle, E. Quandt, M. Wuttig, Ultralow-fatigue shape memory alloy films, Science 348 (2015) 1004–1007.
[15] H. Hou, E. Simsek, T. Ma, N.S. Johnson, S. Qian, C. Cissé, D. Stasak, N.A. Hasan, L. Zhou, Y. Hwang, R. Radermacher, V.I. Levitas, M.J. Kramer, M.A. Zaeem, A.P. Stebner, R.T. Ott, J. Cui, I. Takeuchi, Fatigue–resistant high-performance elastocaloric materials via additive manufacturing, Science 366 (2019) 1116–1121.
[16] T. Baxevanis, A. Cox, D.C. Lagoudas, Micromechanics of precipitated near-equiatomic Ni-rich NiTi shape memory alloys, Acta Mech. 225 (2014) 1167–1185.
[17] T. Bartel, K. Hackl, Multiscale modeling of martensitic phase transformations: On the numerical determination of heterogeneous mesostructures within shape-memory alloys induced by precipitates, Tech. Mech. 30 (2010) 324–342.
[18] O.C. Zienkiewicz, R.L. Taylor, The Finite Element Method: Volume 1- The Basis, Butterworth-Heinemann, Woburn, 2000.
[19] O.C. Zienkiewicz, R.L. Taylor, The Finite Element Method: Volume 2- Solid Mechanics, Butterworth-Heinemann, Woburn, 2000.
[20] Y. Ji, X. Ding, T. Lookman, K. Otsuka, X. Ren, Heterogeneities and strain glass behavior: role of nanoscale precipitates in low-temperature-aged $Ti_{48.7}Ni_{51.3}$ alloys, Phys. Rev. B 87 (2013) 104110.
[21] R. Shi, Y. Wang, Variant selection during α precipitation in Ti_6Al_4V under the influence of local stress a simulation study, Acta Mater. 61 (2013) 6006–6024.
[22] J. Khalil-Allafi, A. Dlouhy, G. Eggeler, Ni_4Ti_3 -precipitation during aging of NiTi shape memory alloys and its influence on martensitic phase transformations, Acta Mater. 50 (2002) 4255–4274.
[23] C.B. Ke, S.S. Cao, X.P. Zhang, Phase field simulation of coherent precipitation of Ni_4Ti_3 particles during stress-assisted aging of a porous NiTi alloy, Modelling Simul. Mater. Sci. Eng. 23 (2015) 055008.
[24] C.B. Ke, S.S. Cao, X.P. Zhang, Phase field modeling of Ni-concentration distribution behavior around Ni_4Ti_3 precipitates in NiTi alloys, Comput. Mater. Sci. 105 (2015) 55–65.
[25] F.L. Tang, X.G. Cheng, W.J. Lu, W.Y. Yu, Premelting of al nonperfect (1 1 1) surface, Physica B. Cond. Matter 405 (2010) 1248–1252.
[26] A. Basak, V.I. Levitas, Phase field study of surface-induced melting and solidification from a nanovoid: effect of dimensionless width of void surface and void size, Appl. Phys. Lett. 112 (2018) 201602.
[27] V.I. Levitas, K. Samani, Size and mechanics effects in surface-induced melting of nanoparticles, Nat. Commun. 2 (2011) 284.
[28] V.I. Levitas, K. Samani, Melting and solidification of nanoparticles: scale effects, thermally activated surface nucleation, and bistable states, Phys. Rev. B 89 (2014) 075427.
[29] V.I. Levitas, M. Javanbakht, Surface tension and energy in multivariant martensitic transformations: Phase-field theory, simulations, and model of coherent interface, Phys. Rev. Lett. 105 (2010) 165701.
[30] V.I. Levitas, M. Javanbakht, Surface-induced phase transformations: multiple scale and mechanics effects and morphological transitions, Phys. Rev. Lett. 107 (2011) 175701.
[31] V.I. Levitas, Effect of the ratio of two nanosize parameters on the phase transformations, Scripta Mater. 192 (2018) 155–162.
[32] H. Jafarzadeh, V.I. Levitas, G.H. Farrahi, M. Javanbakht, Phase field approach for nanoscale interaction between crack propagation and phase transformation, Nanoscal 11 (2019) 22243–22247.
[33] A. Basak, V.I. Levitas, Nanoscale multiphase phase field approach for stress- and temperature-induced martensitic phase transformations with interfacial stresses at finite strains, J. Mech. Phys. Solids 113 (2018) 162–196.
[34] J.H. Lee, S.Y. Lee, Z.H. Lee, H.M. Kim, Ni_3al precipitation behavior in the two-phase (NiAl+Ni_3Al) alloy, High Temp. Mater. Process. 18 (1999) 125–129.
[35] J.A. Sethian, Level Set Methods and Fast Marching Methods : Evolving Interfaces in Computational Geometry, Fluid Mechanics, Computer Vision, and Materials Science, Cambridge University Press, New York, 1999.
[36] R. Yu, P.Y. Hou, First-principles calculations of the effect of Pt on NiAl surface energy and the site preference of Pt, Appl. Phys. Lett. 91 (2007) 011907.
[37] V.I. Levitas, Phase field approach to martensitic phase transformations with large strains and interface stresses, J. Mech. Phys. Solids 70 (2014) 154–189.
[38] I. Steinbach, Phase-field models in materials science, Model. Simul. Mater. Sci. Eng. 17 (2009) 073001.
[39] V.I. Levitas, D.L. Preston, Three-dimensional landau theory for multivariant stress-induced martensitic phase transformations. i. austenite ↔ martensite, Phys. Rev. B 66 (2002) 134206.
[40] V.I. Levitas, D.L. Preston, Three-dimensional landau theory for multivariant stress-induced martensitic phase transformations. II. multivariant phase transformations and stress-space analysis, Phys. Rev. B 66 (2002) 134207.

[41] V.I. Levitas, D.L. Preston, D.W. Lee, Three-dimensional landau theory for multivariant stress-induced martensitic phase transformations. III. alternative potentials, critical nuclei, kink solutions, and dislocation theory, Phys. Rev. B 68 (2003) 134201.
[42] K. Bhattacharya, Microstructure of Martensite: Why It Forms and How It Gives Rise to the Shape-Memory Effect, Oxford University Press, Oxford, 2004.
[43] V.I. Levitas, A.M. Roy, Multiphase phase field theory for temperature-induced phase transformations: formulation and application to interfacial phases, Acta Mater. 105 (2016) 244–257.
[44] S.V. Prikhodko, H. Yang, A.J. Ardel, J.D. Carnes, D.G. Isaak, Temperature and composition dependence of the elastic constants of Ni_3Al, Metall. Mater. Trans. A 30A (1999) 2403–2408.
[45] A.Y. Lozovoi, A. Alavi, M.W. Finnis, Surface energy and the early stages of oxidation of NiAl(110), Comput. Phys. Comm. 137 (2001) 174–194.
[46] W. Tirry, D. Schryvers, High resolution TEM study of Ni_4Ti_3 precipitates in austenitic $Ni_{51}Ti_{49}$, Mater. Sci. Eng. A 378 (2004) 157–160.
[47] W. Bangerth, D. Davydov, T. Heister, L. Heltai, G. Kanschat, M. Kronbichler, M. Maier, B. Turcksin, D. Wells, The deal.II library, version 8.4, J. Numer. Math. 24 (2016) 135–141.
[48] A. Basak, V.I. Levitas, Finite element procedure and simulations for a multiphase phase field approach to martensitic phase transformations at large strains and with interfacial stresses, Comput. Methods Appl. Mech. Eng. 343 (2019) 368–406.
[49] V.I. Levitas, M. Javanbakht, Advanced phase field approach to dislocation evolution, Phys. Rev. B 86 (2012) 140101(R).
[50] M. Javanbakht, V.I. Levitas, Interaction between phase transformations and dislocations at the nanoscale. part 2: Phase field simulation examples, J. Mech. Phys. Solids 82 (2015) 164–185.